Perovskite oxides with Pb at B-site as Li-ion battery anodes

Shahan Atif [a], Anshuman Chaupatnaik [a], Ankit Rao [b], Abhisek Padhy [a], Sridivya Chintha [a], Pavan Nukala [b], Maximilian Fichtner [c,d], Prabeer Barpanda [a,c,d,*]

[a] Faraday Materials Laboratory (FaMaL), Materials Research Centre, Indian Institute of Science, Bangalore 560012, India
[b] Centre for Nano Science and Engineering, Indian Institute of Science, Bangalore 560012, India
[c] Helmholtz Institute Ulm (HIU), Electrochemical Energy Storage, Ulm 89081, Germany
[d] Institute of Nanotechnology, Karlsruhe Institute of Technology (KIT), Karlsruhe 76021, Germany

ARTICLE INFO

Keywords:
Li-ion batteries
Anodes
Perovskites
Conversion
Alloying
Electron microscopy

ABSTRACT

Perovskite ceramic oxides (ABO_3) have emerged as strong contenders against graphite anodes in non-aqueous metal-ion batteries. Exploring perovskites, we studied lithium insertion in barium lead oxide ($BaPbO_3$) and strontium lead oxide ($SrPbO_3$) perovskites, where lead (Pb^{4+}) occupies the B-site. $BaPbO_3$ and $SrPbO_3$, mass produced by solid-state or solution-combustion route, delivered reversible capacities upto 333 mAh/g and 339 mAh/g corresponding to 4.3 and 4.9 lithium uptake, respectively at room temperature. Among them, $BaPbO_3$ showed stable cycling for 50 cycles. Furthermore, at 50 °C, $BaPbO_3$ delivers a first charge capacity of 382 mAh/g (or 5.6 lithium per formula unit) maintaining excellent stability beyond 50 cycles. Ex situ diffraction and microscopy studies confirm charge storage occurs via initial conversion ($Pb^{IV}/Pb^{II} \rightarrow Pb^0$) followed by reversible (de)alloying (Li–Pb) reaction. These results showcase perovskites as a promising family of Li-ion battery anodes.

1. Introduction

In the current scenario of increased environmental pollution and thriving dependency on pocket-sized flexible devices, Li-ion batteries with high energy and power density are of prime research interest around the globe [1-3]. In 1991, SONY® commercialized the Li-ion battery with graphite as an intercalation anode. However, issues with the graphite anode such as low theoretical capacity of 372 mAh/g, risk of Li plating at high currents and poor capacity retention present major hurdles for achieving high-energy-density batteries [4-6]. Better batteries can be built by tailoring anodes to employ additional de(alloying) and conversion mechanisms [7–10]. The alloying based metallic anodes such as Sn show large capacities (4.4 Li per Sn atom) that causes high volume change creating cracks and loss in electrical contact, resulting in poor cycle life performance. In this regard, Sn-based amorphous tin composite oxide (ATCO) glass having two times gravimetric energy density of graphite with cycling performance better than Sn metal, was reported by Miyasaka and was commercialized by Fujifilm Celltech Co. Ltd. as "STALION" cells [9,10,11–13]. Following this, investigations on Sn-based perovskite ($CaSnO_3$) anode showed improved cycling performance by accommodating large volume changes of the Li-Sn alloying reaction inside a buffer matrix (CaO/Li_2O) resulting from irreversible structure decomposition during the first cycle [14]. Thereby, Sn has been studied as the robust anode in various structural forms such as spinel, hollandite and other perovskites based on conversion-alloying reactions [15–19].

Perovskites are a class of compounds used in energy storage with the general formula ABX_3, where X is oxygen (O) or halogen anions positioned at the face center, B-cations are present at the corners with octahedral coordination and A-cations are situated at the body center with 12-fold O coordination. By altering the A and B cations, the material redox behavior and performance can be tuned [20,21]. Thus, unlike the Sn-based perovskite, Ti-based perovskite ($Li_{0.5}La_{0.5}TiO_3$) stores lithium by insertion mechanism via Ti redox, delivering a capacity of 225 mAh/g [5,22]. However, $Na_{0.5}Bi_{0.5}TiO_3$ stores sodium through a conversion-alloying mechanism involving Bi centre [23]. Similarly, the well-known organic-inorganic lead halide perovskites for solar cell can store lithium by Pb alloying involving breakdown of the framework, showing poor structural and cycling stability [24-27]. Recently, our group introduced Pb-based inorganic perovskites $PbTiO_3$ and $PbZrO_3$ as conversion-based anodes for Li-ion and Na-ion batteries accompanied by Pb-alloying center inside perovskite framework [28]. While one may raise concern over toxic nature of Pb, the toxicity associated with Pb-based materials can be circumvented by appropriate materials

* Corresponding author at: Faraday Materials Laboratory (FaMaL), Materials Research Centre, Indian Institute of Science, Bangalore 560012, India.
E-mail address: prabeer@iisc.ac.in (P. Barpanda).

handling/ packaging along with recycling as practiced in case of commercial Pb-acid batteries. It is further reduced in moisture and air stable perovskite frameworks.

Apart from Sn and Ti-based perovskites, Pb-based perovskites form an interesting material system with electrochemical activity stemming from the Pb alloying center. However, Pb containing perovskites where Pb is in B-site of the simple perovskite have not been studied so far for the Li-ion batteries. Herein, for the first time, we successfully demonstrate $BaPbO_3$ and $SrPbO_3$ (now onwards referred as BPO and SPO respectively) as potential anodes for Li-ion batteries. They store Li reversibly via combined conversion-alloying mechanism, which is superior to the one-step conversion or alloying mechanism. $BaPbO_3$ anode delivers a high specific charge capacity of 333 mAh/g (at 5 mA/g) showing good rate performance with negligible capacity fade over 50 cycles. The current work sets up perovskite oxides (ABO_3) as a versatile structure for designing battery anode materials by placing redox active species in both A and B sites. It can pave way to design various perovskites anodes for (post) Li-ion batteries.

2. Experimental section

2.1. Reagents

Lead oxide (PbO, SD Fine Chem., 99%), barium carbonate ($BaCO_3$, SD Fine Chem., 99%), strontium nitrate ($Sr(NO_3)_2$, SD Fine Chem., 99%), lead nitrate ($Pb(NO_3)_2$, SD Fine Chem., 99%), citric acid ($C_6H_8O_7$, SD Fine Chem., 99%), barium nitrate ($Ba(NO_3)_2$, Sigma Aldrich, 99%), Super P carbon black (Alfa Aesar, 99%), sodium Carboxy Methyl Cellulose salt (CMC, Sigma Aldrich, 99%) were used as received.

2.2. Synthesis of $BaPbO_3$ and $SrPbO_3$

Barium lead oxide ($BaPbO_3$), and strontium lead oxide ($SrPbO_3$) were synthesized using conventional solid-state (dry) and solution-combustion (wet) methods. For solid-state method, stoichiometric amounts of PbO, $BaCO_3$, and $Sr(NO_3)_2$ were intimately mixed using mortar and pestle. This mixture was pelletized and was annealed inside a muffle furnace at 900 °C for 4 h (in air) (heating rate = 5 °C/min) without any intermediate grinding. For solution-combustion route, stoichiometric amounts of nitrate oxidizers $Ba(NO_3)_2$, $Sr(NO_3)_2$, $Pb(NO_3)_2$, and citric acid ($C_6H_8O_7$) as fuel were dissolved in distilled water. This mixture was heated at 120 °C leading to the evaporation of excess water, citrate-nitrate complexation, and eventual formation of the combustion intermediate product. It was ground in mortar and pestle and was annealed inside a muffle furnace at 700 °C for 2 h (in air) (heating rate = 2 °C/min) to yield the final products. The overall reactions for the solid-state (SS) and solution-combustion (SC) routes can be written as:

$$Sr(NO_3)_2/BaCO_3 + PbO \rightarrow SrPbO_3/BaPbO_3 + NO_x/CO_x \text{ (SS)}$$

$$Sr(NO_3)_2/Ba(NO_3)_2 + Pb(NO_3)_2 + C_6H_8O_7 \rightarrow SrPbO_3/BaPbO_3 + NO_x + CO_x + H_2O \text{ (SC)}$$

2.3. Physical characterizations

X-ray powder diffraction was performed with a Panalytical Empyrean X-ray diffractometer equipped with a Cu K_α source ($\lambda = 1.5405$ Å) (operating at 40 kV/30 mA). Inorganic Crystal Structure Database (ICSD) was used as reference. Rietveld analysis was performed using the GSAS software with EXPGUI graphical interface [29]. VESTA-3 software was used for the structural illustration [30]. The powder morphology was inspected using a field emission scanning electron microscope (FESEM) (Ultra55, Carl Zeiss AG) equipped with a thermal field emission source (W) operating at 0.1–30 kV. Gold sputtering was carried out (for 120 s) on the electronically insulating powder sample to ensure electronic conductivity. Further, high-resolution transmission electron microscopy (HRTEM) images, selected area diffraction patterns (SAED) and high-angle annular dark field-scanning transmission electron micrographs (HAADF-STEM) of powder samples were collected employing an FEI Tecnai TITAN Themis microscope operating at 300 kV. Scanning transmission electron microscopy energy dispersive X-ray spectroscopy (STEM EDS) was acquired for the elemental mapping of the as-synthesized sample in HAADF-STEM mode. For TEM analysis, powder samples were dispersed in hexane, sonicated to ensure homogeneous dispersion and drop cast onto carbon film mesh copper grids (EMS). Fourier transform infrared (FTIR) spectrum was recorded in the spectral range of 4000–650 cm^{-1} with a PerkinElmer instrument in attenuated total reflectance (ATR) mode. Simultaneous thermal analysis (thermogravimetry coupled with differential scanning calorimetry or TGA-DSC) of intermediate powder of BPO and SPO was performed with a Perkin Elmer STA-8000 unit in the temperature range of 30–900 °C (heating rate = 10 °C/min under N_2 flow at rate of 50 ml/min).

2.4. Electrochemical measurements

The electrochemical performance was examined in CR2032-type coin cells using the copper foil coated with active material as the working electrode and (Li/Na) metal foils as the counter as well as reference electrode, respectively. Electrode inks were prepared by mixing active material, Super P carbon black and sodium Carboxy Methyl Cellulose salt (CMC) with mortar and pestle in weight ratios of 70:20:10, using distilled water as solvent and copper foil as current collector. Electrode inks were drop cast on precut SS304 or battery grade Cu foil. The electrodes were dried under vacuum oven at 60 °C overnight to remove any moisture and were transferred into an Ar-filled glovebox (MBraun LabStar GmbH, O_2 and H_2O levels <0.5 ppm). Coin-type half cells were assembled inside the glovebox. A glass microfiber filter (Whatman, grade GF/C) was used as a separator. 1 M $LiPF_6$ dissolved in 1:1:3 v/v% of ethylene carbonate/propylene carbonate/dimethyl carbonate (EC/PC/DMC) was used as the lithium electrolyte (Sigma Aldrich, 99%). 1 M $NaPF_6$ dissolved in 0.45:0.45:0.1 v/v% EC/PC/DMC was used as the sodium electrolyte. Cells were galvanostatically (dis) charged with a Neware BTS-4000 (Shenzhen, China) battery tester in the voltage window of 0.01 V to upper cut off (1.5 V) without any rest time in between charge and discharge. Cyclic voltammograms (CV) were recorded at a scan rate of 0.6 mV/s and potentiostatic intermittent titration technique (PITT) was conducted at a current density of 1 mA/g using a Bio-Logic BCS 805/810 (Claix, France) automatic battery cycler.

2.5. Ex situ analysis

For ex situ analysis, cycled swageloks were disassembled inside the glovebox, and the recovered electrodes were washed using diethyl carbonate (DEC, anhydrous, ≥99%) followed by dimethyl carbonate (DMC, anhydrous, ≥99%) and were dried inside the glovebox. Electrodes were cut for further ex situ characterization. For TEM study, electrode materials were scratched from the washed electrode, were dispersed in hexane and sonicated to ensure proper dispersion. It was drop cast on TEM grids and dried overnight before examination. The oxidation states of pristine and ex situ samples were analysed by X-ray photoelectron spectroscopy (XPS) employing a Thermo-Scientific Ka XPS instrument operating at 12 kV/6 mA. The binding energy of 284.6 eV of main carbon signal was considered as the reference for the calibration. The resulting XPS spectra were fitted using CASA software after Shirley background subtraction. Ex situ X-ray diffraction (XRD) patterns were recorded as discussed in Section 2.3.

3. Results and discussion

The SPO and BPO perovskites were synthesized by both combustion

and solid-state methods. Simultaneous thermal analysis (TGA-DSC) performed on the combustion intermediate complexes of BPO and SPO (from 30~900 °C, Fig. S1) revealed a peak around ~600 °C, indicating the formation of the target compounds, which remained stable till 900 °C. Taking clue from the thermal analysis, the intermediate powder was annealed at 700 °C to obtain the desired product phases [31]. The X-ray diffraction patterns of $BaPbO_3$ (BPO) and $SrPbO_3$ (SPO), prepared using both solid-state and solution combustion synthesis, confirmed the formation of the target perovskites without any impurity (Fig. S2). Rietveld refinement of the powder XRD patterns of BPO (Fig. 1a) and SPO (Fig. 1b) using GSAS software confirmed the formation of orthorhombic crystal structures for both phases, with space groups *Ibmm* (BPO) and *Pnma* (SPO) (Inset, Fig. 1a,b). The crystallographic parameters for BPO and SPO are provided in Table S1 and S2 respectively. SEM micrographs (Fig. S3) revealed agglomerated micrometric particle morphology, with smaller particle sizes observed for both BPO and SPO prepared by solution combustion synthesis as compared to solid-state method. The bright-field high-resolution transmission electron microscope (HRTEM) images of BPO (Fig. 1c) and SPO (Fig. 1e) revealed the crystalline nature of the materials, depicting (100) and (110) planes with interplanar spacings of 4.32 Å and 6.03 Å, respectively. Their crystallinity was further confirmed by the selected area electron diffraction (SAED) patterns which could be indexed to [311] zone axis in BPO (Fig. 1d), while showing (100) and (110) planes in SPO (Fig. 1f). Additionally, the homogeneous elemental distribution in BPO (Ba, Pb, O) and SPO (Sr, Pb, O) was confirmed by energy-dispersive X-ray spectroscopy (EDS) analysis in high-angle annular dark-field scanning transmission electron microscopy (HAADF-STEM) mode (Fig. 1g-n).

Fig. S4a,b show the X-ray photoelectron (XPS) spectra of pristine BPO and SPO, revealing signals of Pb 4*f*, Ba 3*d*, Sr 3*d*, O 1*s* and C 1*s* located at 138 eV, 780 eV, 135 eV, 531 eV, and 285 eV respectively assuring the presence of Pb^{4+}, Pb^{2+}, Ba^{2+} and Sr^{2+} species in the BPO and SPO perovskites. More importantly, the XPS spectra of BPO and SPO indicate these materials are not standard $A^{2+}B^{4+}(O^{2-})_3$ perovskites [32]. Instead, they are $A^{2+}B^{2+/4+}(O^{2-})_2O^{2-}$ as indicated from the binding energies of the O 1*s* peaks at 531.1 and 528.7 eV, which are close to reference O 1*s* binding energies of 531.1 eV and 528.7 eV for peroxide BaO_2 and oxide O^{2-}, respectively [31]. The O 1*s* spectra of BPO and SPO, thus correspond to PbO, BaO_2 and SrO_2 showing characteristic features of O^{2-} and O_2^{2-}, respectively (Fig. S4c). This variation of valence and presence of O_2^{2-} in BPO and SPO may be described by the reactions (1) which occurs in oxides where the oxidation number of the metal ion (here, Pb) differs by two [33]:

$$Pb^{4+} + 2O^{2-} \leftrightarrow Pb^{2+} + O_2^{2-} \quad (1)$$

Fig. S4d illustrates the Ba $3d_{5/2}$ peak, which underwent deconvolution into two discernible peaks at 779.5 eV and 794.9 eV, attributed to Ba^{2+} in the $BaPbO_3$ compound. In Fig. S4e, the SPO spectra displays the Sr $3d_{5/2}$ peak resolved into two distinct peaks at 133.2 eV and 134.9 eV, similarly confirming the presence of Sr^{2+} ions. Fig. S4f exhibits the XPS spectra of Pb $4f_{7/2}$ and $4f_{5/2}$ for both SPO and BPO. The Pb $4f_{7/2}$ and $4f_{5/2}$ peaks could also be deconvoluted into two major peaks. The presence of Pb^{4+} was unequivocally confirmed from the Pb XPS spectra, with Pb $4f_{7/2}$ and $4f_{5/2}$ peaks detected at 137.8 eV and 142.6 eV, respectively. Additionally, two smaller peaks at lower energies of 136.9 eV and 141.6 eV were observed, attributed to Pb^{2+} ions, as documented in the literature [34,35].

The as prepared micrometric-sized BPO and SPO samples were tested as anodes versus Li/Na counter electrodes within a half-cell architecture as shown by their galvanostatic charge-discharge profiles in Fig. 2. Notably, the first discharge curve exhibits a significant irreversible capacity, suggesting the initial step involves the irreversible conversion of

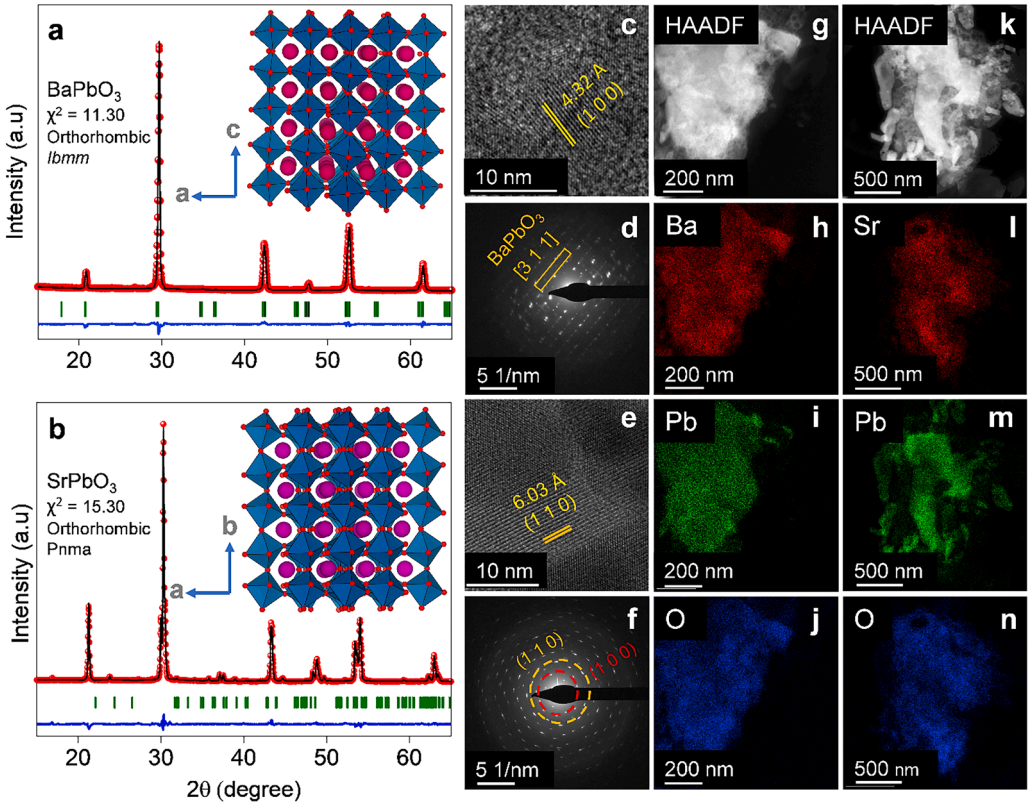

Fig. 1. Rietveld refined XRD (Cu Kα, λ 1.5405 Å) patterns of (a) $BaPbO_3$ (BPO) and (b) $SrPbO_3$ (SPO) perovskites. Inset shows the orthorhombic crystal structure of BPO (space group: Ibmm) and SPO (space group: Pnma) projected along the [001] and [010] direction. PbO_6 octahedra, Ba, Sr and O are denoted by dark blue, wine, pink and red colours respectively. (c,e) HRTEM images, (d,f) SAED patterns of BPO and SPO. Representative annular dark field HAADF images and the corresponding elemental mapping revealing (g-j) BPO and (k-n) SPO having uniform distribution of all constituent elements (Ba, Sr, Pb, O).

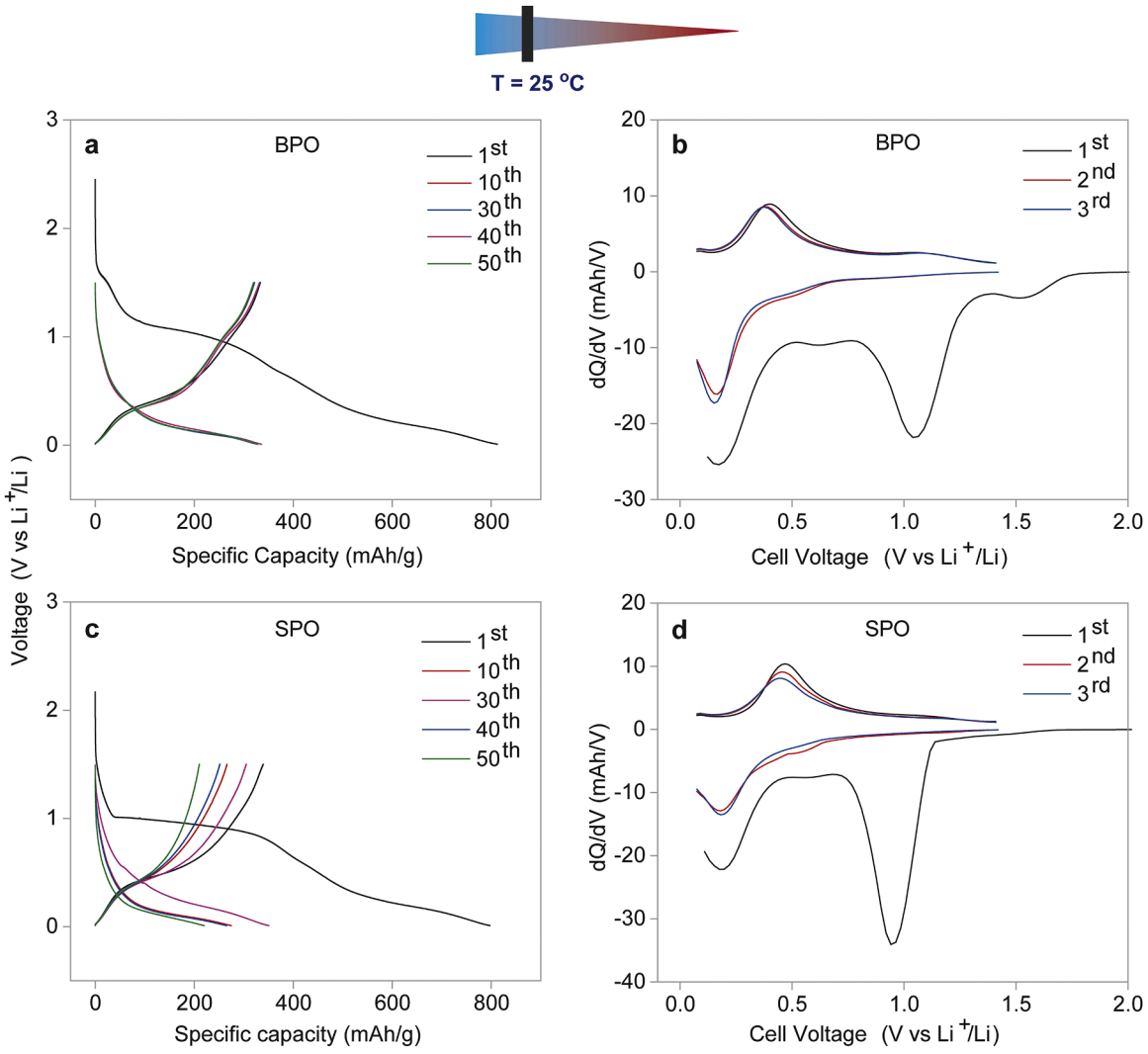

Fig. 2. Galvanostatic discharge-charge profiles of (a) BPO and (c) SPO vs Li shown till 50 cycles at 5 mA/g current density. Corresponding differential capacity curve (dQ/dV) of (b) BPO and (d) SPO shown for 3 cycles at 5 mA/g current density.

the structure and the formation of Pb metal, as described by reaction (2).

$$APbO_3 + 4Li^+ + 4e^- \leftrightarrow Pb + AO_2 + Li_2O \ (A = Ba, Sr) \quad (2)$$

Cyclic voltammetry (CV) analysis shows that the first cycle is distinctively different from subsequent cycles (Fig. S5a). During this initial cycle as the parent structure breaks down, Pb (IV) takes four electrons reducing to electroactive Pb metal that disperses within the inactive matrix of Li_2O and SrO_2/BaO_2 peroxides. This initial structural transformation plays a pivotal role in subsequent cycling as the dispersed metal (per)oxides cushion volume expansion and prevent particle cracking thereby preserving electrode integrity. In Fig. 2b,d, the dQ/dV curves reveal two distinct voltage steps at approximately ~1.04 V and ~0.62 V, followed by a flat plateau at ~0.17 V. The peak at ~1.04 V corresponds to the structural breakdown, while the peak at ~0.17 V signifies the alloying reaction of Pb with Li forming Li_xPb alloys ($1.0 < x < 4.4$) [36,37]. The peak at ~0.62 V is attributed to the formation of the solid electrolyte interface (SEI) film [38], which is absent in subsequent cycles confirming SEI formation only during the initial discharge. Fig. 2a,d depict the discharge-charge profiles, with the first discharge and charge capacities of BPO and SPO measuring approximately ~811 mAh/g, ~797 mAh/g and ~333 mAh/g, ~339 mAh/g, respectively, corresponding to initial columbic efficiency of only ~41% and ~42%. Such relatively low initial coulombic efficiencies are common in conversion and alloying-type anodes. However, the coulombic efficiency increases to ~95% and ~96% in the second cycle (Fig. S5b), suggesting that the second step is solely reversible (de)alloying, as expressed by reaction (3).

$$Pb + xLi^+ + xe^- \leftrightarrow Li_xPb \ (x \leq 4.4) \quad (3)$$

From the dQ/dV plot, it is evident that peaks at ~0.15 V during discharge and ~0.37 V during charge signify the reversible formation of Li_xPb and $Li_{22}Pb_5$ alloys after first discharge. The charge capacity arises from the dealloying reaction of Pb from $Li_{22}Pb_5$.

It is noteworthy that commercial lithium-ion batteries (LIBs) operate effectively within a temperature range of 20 to 55 °C globally. Fig. 3 illustrates the electrochemical performance of BPO and SPO cycled at an elevated temperature of 50 °C. BPO exhibits a notably high first reversible charge capacity of 382 mAh/g and a second reversible discharge capacity of 422 mAh/g, as depicted in Fig. 3a. Similarly, SPO demonstrates a high first reversible charge capacity of 380 mAh/g and a second reversible discharge capacity of 400 mAh/g, as outlined in Fig. 3c. At 50 °C, the charge storage mechanism remains consistent with room temperature, as indicated by the dQ/dV plots of BPO (Fig. 3b) and SPO (Fig. 3d). This consistency across temperatures underscores the robustness and stability of BPO and SPO as potential anode materials for high-temperature alkali-ion battery applications. Further, Fig. S5c presents the potentiostatic titration technique (PITT) curve of BPO, where the current decay around ~1.04 V and ~0.17 V exhibits a bell-shaped

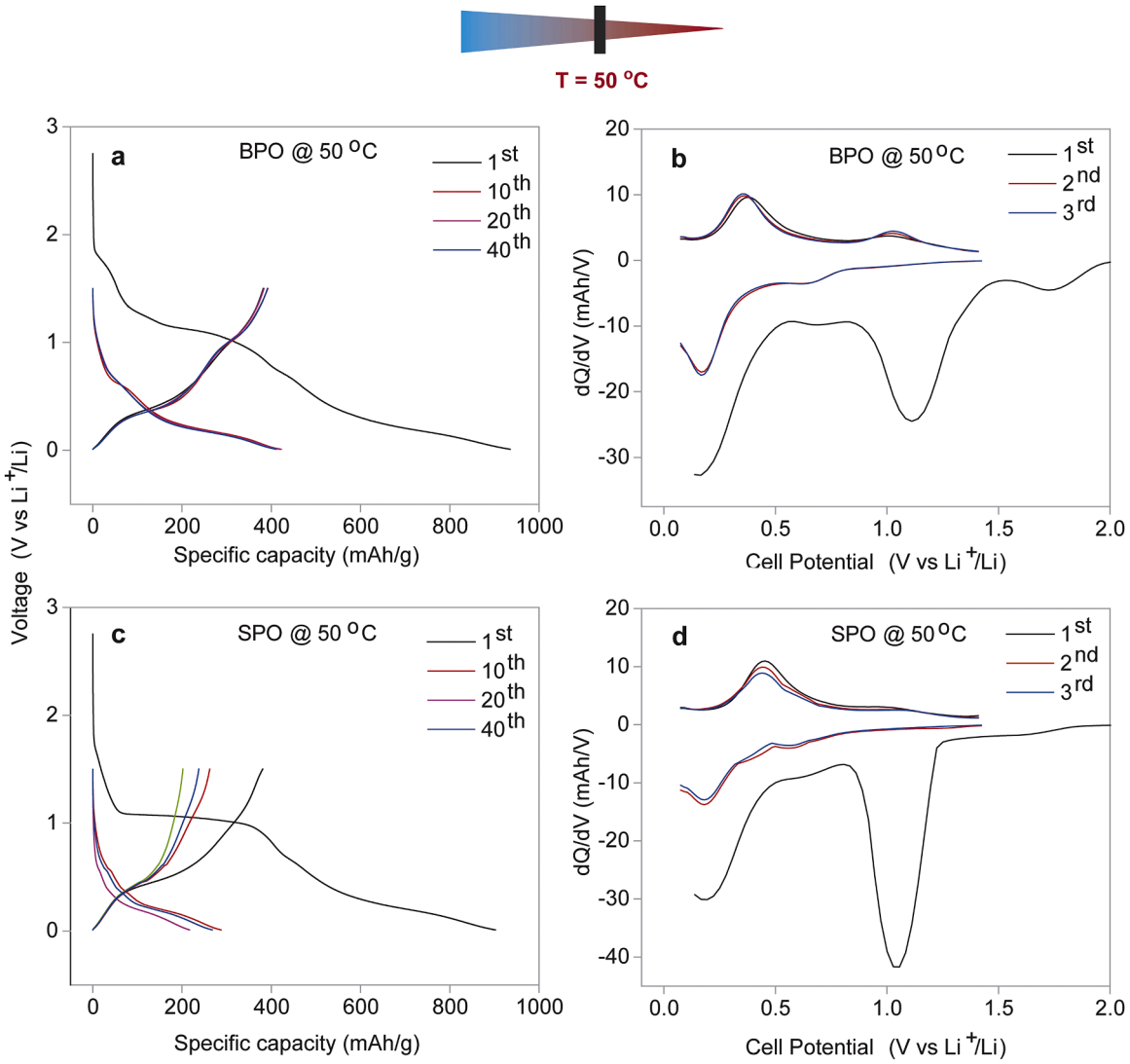

Fig. 3. Galvanostatic discharge-charge profiles of (a) BPO and (c) SPO vs Li shown till 50 cycles at 5 mA/g current density at 50 °C. Corresponding differential capacity curve (dQ/dV) of (b) BPO and (d) SPO shown for 3 cycles at 5 mA/g current density at 50 °C.

response, corresponding to the phase change of BPO and Li_xPb alloy formation [39]. The cycling stability of BPO and SPO at both room temperature and high temperature is depicted in Fig. S6. BPO maintains a high specific capacity of 328 mAh/g at room temperature (Fig. S6a) and 401 mAh/g at high temperature (Fig. S6b) even after 50 cycles. Conversely, SPO at 50 °C exhibits a performance comparable to that at room temperature (Fig. S6c). Importantly, BPO demonstrates excellent cycle life performance under both room and high temperatures.

Rate capability is crucial for ensuring the superior performance of batteries. As illustrated in Fig. S6d, the BPO electrode delivers specific capacities of 370, 296, 259, 182, 131, and 93 mAh/g at current densities of 0.005, 0.02, 0.05, 0.1, 0.5, and 1.0 A/g, respectively. Notably, as high as ~306 mAh/g of reversible capacity is restored when the current density is switched back from 1 to 0.005 A/g. With the success of the Li-ion battery, the electrochemical performance of BPO and SPO was also evaluated for the Na-half cell (Fig. S7). While initial activity was observed, rapid capacity degradation was noticed from the initial cycling. The larger size of Na^+ ions compared to Li^+ ions may induce significant volume changes in the Na-ion battery, leading to capacity fading and poor electrochemical performance.

The precise (de)lithiation mechanism of perovskite BPO anode was investigated using a comprehensive set of ex situ measurements. These included high-resolution transmission electron microscopy (HR-TEM), selected area electron diffraction (SAED), X-ray photoelectron spectroscopy (XPS), and X-ray diffraction (XRD), carried out at various states of (dis)charge spanning from 0.01 V to 1.5 V. Following the complete discharge process (involving conversion and alloying) of BPO to 0.01 V, the conversion of the pristine phase to Pb or Li_xPb phase was confirmed through TEM micrographs and the presence of discrete spots in the SAED pattern (Fig. 4a-c). Additionally, the initial particles underwent transformation into smaller particles, as evidenced by the SEM micrographs of BPO discharged to 0.01 V (BPO-1D-0.01 V) (Fig. S3e). After the first charge/dealloying of BPO (BPO-1C-1.5 V), Pb particles dispersed within the amorphous BaO_2 peroxide matrix were clearly observed in the TEM analysis (Fig. 4d-f). To investigate the surface elements following post-charge and discharge, ex situ XPS spectra were collected (Fig. 4g-i). At the end of the first discharge (1D-0.01 V) and first charge (1C-1.5 V) of BPO perovskite, PbO disappeared from the O 1*s* spectra of BPO (Fig. 4g), while the peaks corresponding to BaO_2, Li_2O and Li_2CO_3 peaks remained, confirming the conversion of the pristine phase of BPO to BaO_2 and a Li_2O matrix containing smaller Pb particles. Furthermore, the Li 1*s* spectra revealed the presence of Li_2O and Li_2CO_3, as illustrated in Fig. 4h [40]. Electrolyte decomposition resulted in a Li_2CO_3 peak, and a slight shift towards higher binding energy after post-discharge and charge, corresponding to 780 eV, confirmed the presence of BaO_2 matrix as Ba^{2+}, as indicated in Fig. 4i. Thus, the ex situ XPS studies confirmed

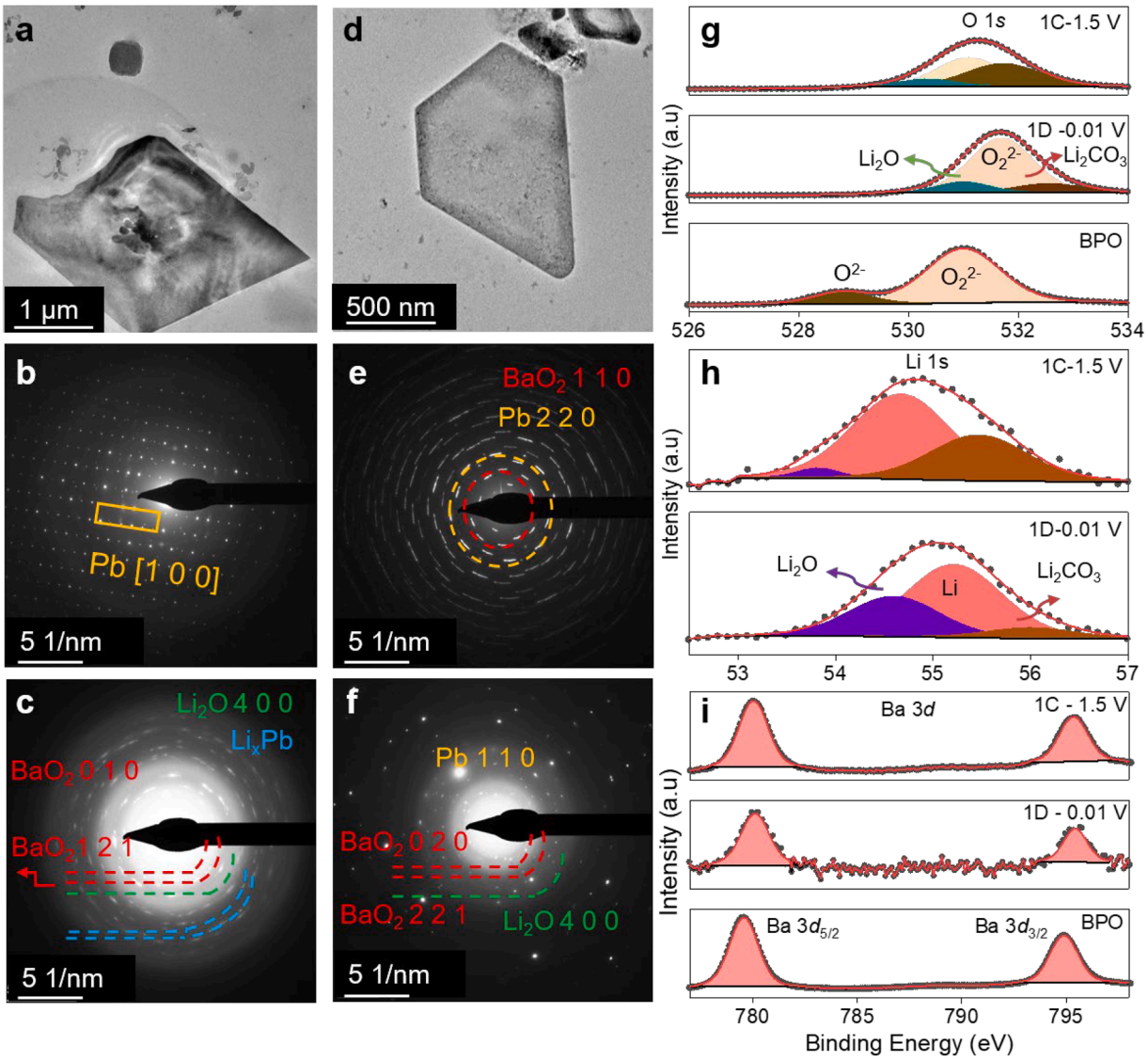

Fig. 4. Ex situ TEM analysis of BPO anode samples after 1st discharge to 0.01 V vs Li: (a) Bright field TEM micrograph and (b,c) SAED patterns confirming Pb and BaO_2, Li_2O, Li_xPb phase formation. Ex situ TEM study of BPO samples after 1st charge to 1.5 V vs Li: (d) Bright field TEM micrographs, (e,f) SAED pattern confirming Pb, BaO_2, and Li_2O phase formation. Comparative analysis of ex situ XPS spectra of pristine BPO, after 1st discharge to 0.01 V and 1st charge to 1.5 V vs Li: (g) O 1*s* spectra, (h) Li 1*s* spectra, and (i) Ba 3*d* spectra.

the dispersion of electroactive Pb particles in BaO_2 and Li_2O matrix, aligning with the TEM analysis. These results highlight the crucial role of inactive matrices such as BaO_2 for buffering volume changes and ensuring high cycling stability [28]. The FT-IR spectra of cycled BPO, recorded in attenuated total reflection (ATR) mode in open air, are depicted in Fig. S8. The inset of Fig. S8 displays the peak at 669 cm^{-1}, corresponding to Pb–O vibration, confirming the presence of the BPO phase. The reactivity of Pb particles increased due to the small particle size of Pb after cycling, resulting in the Pb–O vibration peak [41]. The FT-IR spectra confirmed the smaller size of Pb particles, consistent with the SEM image of BPO at the end of the first discharge.

In Fig. 5, ex situ XRD patterns obtained at various (dis)charged states shed light on the Li^+ storage mechanism within the BPO and SPO perovskite anodes. Upon initial discharge from 1.67 to 1.03 V, the XRD peaks of the pristine material shifted to lower angles, indicating the insertion of lithium into the BPO lattice, ultimately leading to structural collapse between the discharge states of BPO to 1.03 V and 0.75 V, as depicted in Fig. 5a. After the first complete discharge (1D-0.01), the prominent signature peaks of BPO (Fig. 5b) and SPO (Fig. 5c) diminished, while new peaks emerged, corresponding to metallic Pb and/or various Li_xPb alloy formations (such as Li_8Pb_3, $Li_{22}Pb_5$, LiPb, $Li_{10}Pb_3$), as confirmed by the Li–Pb binary phase diagram [42]. For instance, the Li_8Pb_3 phase corresponds to peaks at 2θ values of 62.1°, while peaks at 2θ values of 31.3°, 36.2°, and 52.2° are attributed to metallic Pb or different Li_xPb phases (Fig. 5a) [43,44]. The Li–Pb binary alloy obtained after full Pb lithiation is $Li_{22}Pb_5$. Additionally, at the end of the first complete charge (delithiation) (1C-1.5 V) of BPO and SPO, the appearance of peaks corresponding to metallic Pb confirmed the charge capacity attributed to the delithiation of Pb from Li_xPb alloy (Fig. 5). Electrochemical impedance spectroscopy (EIS) was examined for cycled BPO (Fig. S9a) and SPO electrodes (Fig. S9b). The comparative Nyquist plot of BPO and SPO at open circuit voltage (OCV), first complete discharge (1D-0.01 V), and first complete charge (1C-1.5 V) (inset of Fig. S9b) revealed the charge-transfer resistance (R_{ct}) of BPO is lower than that of SPO at OCV, suggesting better capacity retention of BPO than SPO. At the end of the first discharge of BPO and SPO, two semi-circles were observed, indicating the formation of the solid electrolyte interface (SEI). In contrast, only one semi-circle was observed at the end of the first charge, suggesting that the SEI has stabilized during the first discharge. Further, the lower charge transfer resistance is

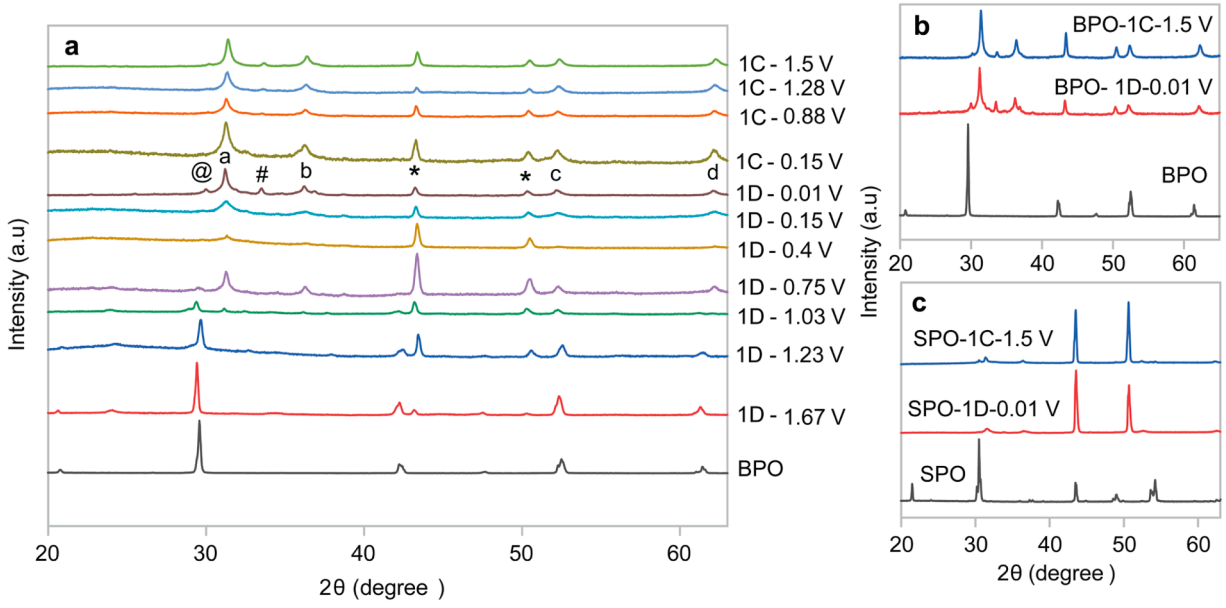

Fig. 5. (a) Ex situ X-ray diffraction patterns of BPO electrodes at different states of discharge and charge (where * Cu, @ PbO, # Li_2O *a* $Li_{22}Pb_5$/Pb, *b* LiPb/Pb, *c* $Li_{10}Pb_3$/Pb, *d* Li_8Pb_3). Ex situ X-ray diffraction patterns of (b) BPO and (c) SPO electrodes after 1st discharge to 0.01 V and 1st charge to 1.5 V for Li-ion half-cells. Cu peaks are from the current collector substrate.

attributed to the dealloying process at the end of the first charge, as the Li conductivity is higher after the alloying process of Li_xPb [45].

4. Conclusions

In summary, two single perovskite (ABO_3) oxides $BaPbO_3$ and $SrPbO_3$ with Pb at B-site were synthesized via solid-state and solution combustion routes. They were demonstrated for the first time as a novel class of conversion-alloy type anodes for Li-ion batteries. Employing suites of ex situ diffraction and spectroscopic tools, the charge storage mechanism was found to predominantly occur via a (de)alloying process within $BaPbO_3$ and $SrPbO_3$ anodes. $BaPbO_3$ and $SrPbO_3$ exhibited high first reversible charge capacities of 333 and 339 mAh/g, respectively. Notably, $BaPbO_3$ demonstrates superior high-rate performance and excellent cycling stability at both room and high temperatures, thus emphasizing its feasibility as a promising anode material for Li-ion batteries. This study elucidates the potential of ABO_3 perovskite oxides, such as $BaPbO_3$ and $SrPbO_3$, for charge storage via the conversion-alloying mechanism. Complementing our earlier work on $PbTiO_3$/$PbZrO_3$ perovskites with Pb in A site, the current work on perovskites with Pb in B site opens avenues to design various (non)oxide perovskite frameworks as potential battery anode materials for (post) Li-ion batteries.

Appendix A. Supplementary data

Supporting information file is provided.

CRediT authorship contribution statement

Shahan Atif: Writing – original draft, Methodology, Formal analysis, Data curation. **Anshuman Chaupatnaik:** Writing – original draft, Formal analysis, Data curation, Conceptualization. **Ankit Rao:** Writing – original draft, Formal analysis, Data curation. **Abhisek Padhy:** Writing – original draft, Formal analysis, Data curation. **Sridivya Chintha:** Formal analysis, Data curation. **Pavan Nukala:** Writing – review & editing, Formal analysis. **Maximilian Fichtner:** Writing – review & editing, Project administration. **Prabeer Barpanda:** Writing – review & editing, Resources, Project administration, Funding acquisition, Formal analysis, Conceptualization.

Declaration of competing interest

The authors declare that they have no known competing financial interests or personal relationships that could have appeared to influence the work reported in this paper.

Data availability

Data will be made available on request.

Acknowledgements

The current work was financially supported by the Department of Science and Technology (Government of India) under the Core Research Grant (CRG/2022/000963). S.A. and S.C. thank Prime Minister Research Fellowships from the Ministry of Human Resource Development (MHRD, Government of India). A.C. and A.R. are grateful to the Ministry of Human Resource Development (MHRD) for fellowships. A.C. acknowledges Centre Franco-Indien pour la Promotion de la Recherche Avancee (CEFIPRA) for a Raman-Charpak Fellowship-2019 and Prof. Jean-Marie Tarascon for hosting him at the Collège de France, Paris. A.P. is grateful to Indian Institute of Science for an Institute of Eminence postdoctoral fellowship (R(HR)(IoE-IISc)(PDF)(MRC)(80010824) 3101). P.B. is grateful to the Alexander von Humboldt Foundation (Bonn, Germany) for a 2022 Humboldt fellowship for experienced researchers.

References

[1] S.J. Clark, D. Wang, A.R. Armstrong, P.G. Bruce, $Li(V_{0.5}Ti_{0.5})S_2$ as a 1 V lithium intercalation electrode, Nat. Commun. 7 (2016) 5–11, https://doi.org/10.1038/ncomms10898.

[2] S. Bashir, P. Hanumandla, H.Y. Huang, J.L. Liu, Nanostructured materials for advanced energy conversion and storage devices: safety implications at end-of-life disposal, Nanostruct. Mater. 4 (2018) 517–542, https://doi.org/10.1007/978-3-662-56364-9_18.

[3] M.K. Song, S. Park, F.M. Alamgir, J. Cho, M. Liu, Nanostructured electrodes for lithium-ion and lithium-air batteries: the latest developments, challenges, and perspectives, Mater. Sci. Eng. R Reports. 72 (2011) 203–252, https://doi.org/10.1016/j.mser.2011.06.001.

[4] Y.P. Wu, C. Jiang, C. Wan, R. Holze, Modified natural graphite as anode material for lithium ion batteries, J. Power Sources. 111 (2002) 329–334, https://doi.org/10.1016/S0378-7753(02)00349-X.

[5] L. Zhang, X. Zhang, G. Tian, Q. Zhang, M. Knapp, H. Ehrenberg, G. Chen, Z. Shen, G. Yang, L. Gu, F. Du, Lithium lanthanum titanate perovskite as an anode for lithium-ion batteries, Nat. Commun. 11 (2020) 1–8, https://doi.org/10.1038/s41467-020-17233-1.

[6] M. Petzl, M. Kasper, M.A. Danzer, Lithium plating in a commercial lithium-ion battery - A low-temperature aging study, J. Power Sources. 275 (2015) 799–807, https://doi.org/10.1016/j.jpowsour.2014.11.065.

[7] A. Ulus, Y. Rosenberg, L. Burstein, E. Peled, Tin alloy-graphite composite anode for lithium-ion batteries, J. Electrochem. Soc. 149 (2002) A635, https://doi.org/10.1149/1.1469029.

[8] I.A. Courtney, W.R. McKinnon, J.R. Dahn, On the aggregation of Tin in SnO composite glasses caused by the reversible reaction with lithium, J. Electrochem. Soc. 146 (1999) 59–68, https://doi.org/10.1149/1.1391565.

[9] I.A. Courtney, J.R. Dahn, Electrochemical and in situ x-ray diffraction studies of the reaction of lithium with tin oxide composites, J. Electrochem. Soc. 144 (1997) 2045–2052, https://doi.org/10.1149/1.1837740.

[10] Y. Idota, T. Kubota, A. Matsufuji, Y. Maekawa, T. Miyasaka, Tin-based amorphous oxide: a high-capacity lithium-ion-storage material, Science 276 (1997) 1395–1397, https://doi.org/10.1126/science.276.5317.1395.Y.

[11] I.A. Courtney, J.R. Dahn, Key factors controlling the reversibility of the reaction of lithium with SnO_2 and Sn_2BPO_6 glass, J. Electrochem. Soc. 144 (1997) 2943–2948, https://doi.org/10.1149/1.1837941.

[12] D. Aurbach, A. Nimberger, B. Markovsky, E. Levi, E. Sominski, A. Gedanken, Nanoparticles of SnO produced by sonochemistry as anode materials for rechargeable lithium batteries, Chem. Mater. 14 (2002) 4155–4163, https://doi.org/10.1021/cm021137m.

[13] M. Behm, J.T.S. Irvine, Influence of structure and composition upon performance of tin phosphate based negative electrodes for lithium batteries, Electrochim. Acta. 47 (2002) 1727–1738, https://doi.org/10.1016/S0013-4686(02)00017-8.

[14] N. Sharma, K.M. Shaju, G.V. Subba Rao, B.V.R. Chowdari, Sol-gel derived nano-crystalline $CaSnO_3$ as high capacity anode material for Li-ion batteries, Electrochem. Commun. 4 (2002) 947–952, https://doi.org/10.1016/S1388-2481(2)00495-2.

[15] Z. Wang, Z. Wang, W. Liu, W. Xiao, X.W. Lou, Amorphous $CoSnO_3$@C nanoboxes with superior lithium storage capability, Energy Environ. Sci. 6 (2013) 87–91, https://doi.org/10.1039/c2ee23330d.

[16] Y. Sharma, N. Sharma, G.V. Subba Rao, B.V.R. Chowdari, Lithium-storage and cycleability of nano-$CdSnO_3$ as an anode material for lithium-ion batteries, J. Power Sources. 192 (2009) 627–635, https://doi.org/10.1016/j.jpowsour.2009.02.096.

[17] N. Sharma, J. Plévert, G.V. Subba Rao, B.V.R. Chowdari, T.J. White, Tin oxides with hollandite structure as anodes for lithium-ion batteries, Chem. Mater. 17 (2005) 4700–4710, https://doi.org/10.1021/cm0505042.

[18] P.A. Connor, J.T.S. Irvine, Novel tin oxide spinel-based anodes for Li-ion batteries, J. Power Sources. 97–98 (2001) 223–225, https://doi.org/10.1016/S0378-7753(01)00545-6.

[19] M. Hu, Y. Jiang, W. Sun, H. Wang, C. Jin, M. Yan, Reversible conversion-alloying of Sb_2O_3 as a high-capacity, high-rate, and durable anode for sodium ion batteries, ACS Appl. Mater. Interfaces. 6 (2014) 19449–19455, https://doi.org/10.1021/am505505m.

[20] B. Sun, S. Mao, S. Zhu, G. Zhou, Y. Xia, Y. Zhao, Improved rate and cycling performances of electrodes based on $BiFeO_3$ nanoflakes by compositing with organic pectin for advanced rechargeable na-ion batteries, ACS Appl. Nano Mater. 1 (2018) 1291–1299, https://doi.org/10.1021/acsanm.8b00011.

[21] H. Lei, D. Hardy, F. Gao, Lead-free double perovskite $Cs_2AgBiBr_6$: fundamentals, applications, and perspectives, Adv. Funct. Mater. 31 (2021), https://doi.org/10.1002/adfm.202105898.

[22] C. Hua, X. Fang, Z. Wang, L. Chen, Lithium storage in perovskite lithium lanthanum titanate, Electrochem. Commun. 32 (2013) 5–8, https://doi.org/10.1016/j.elecom.2013.03.038.

[23] K.K. Bharathi, B. Moorthy, H.K. Dara, L. Durai, D.K. Kim, Electrochemical properties of $Na_{0.5}Bi_{0.5}TiO_3$ perovskite as an anode material for sodium ion batteries, J. Mater. Sci. 54 (2019) 13236–13246, https://doi.org/10.1007/s10853-019-03834-9.

[24] D. Ramirez, Y. Suto, N.C. Rosero-Navarro, A. Miura, K. Tadanaga, F. Jaramillo, Structural and electrochemical evaluation of three- and two-dimensional organohalide perovskites and their influence on the reversibility of lithium intercalation, Inorg. Chem. 57 (2018) 4181–4188, https://doi.org/10.1021/acs.inorgchem.8b00397.

[25] L. Zhang, J. Miao, J. Li, Q. Li, Halide perovskite materials for energy storage applications, Adv. Funct. Mater. 30 (2020) 1–20, https://doi.org/10.1002/adfm.202003653.

[26] H.R. Xia, W.T. Sun, L.M. Peng, Hydrothermal synthesis of organometal halide perovskites for Li-ion batteries, Chem. Commun. 51 (2015) 13787–13790, https://doi.org/10.1039/c5cc05053g.

[27] J.A. Dawson, A.J. Naylor, C. Eames, M. Roberts, W. Zhang, H.J. Snaith, P.G. Bruce, M. Saiful Islam, Mechanisms of lithium intercalation and conversion processes in organic-inorganic halide perovskites, ACS Energy Lett 2 (2017) 1818–1824, https://doi.org/10.1021/acsenergylett.7b00437.

[28] A. Chaupatnaik, P. Barpanda, Perovskite lead-based oxide anodes for rechargeable batteries, Electrochem. Commun. 127 (2021) 107038, https://doi.org/10.1016/j.elecom.2021.107038.

[29] J. Rodriguez-Carvajal, Recent advances in magnetic structure determination by neutron powder diffraction, Phys. B. 192 (1993) 55–69, https://doi.org/10.1016/0921-4526(93)90108-I.

[30] K. Momma, F. Izumi, VESTA 3 for three-dimensional visualization of crystal, volumetric and morphology data, J. Appl. Cryst. 44 (2011) 1272–1276, https://doi.org/10.1107/S0021889811038970.

[31] T. Tabari, H. Tavakkoli, P. Zargaran, D. Beiknejad, Fabrication of perovskite-type oxide $BaPbO_3$ nanoparticles and their efficiency in photodegradation of methylene blue, South African J. Chem. 65 (2012) 239–244.

[32] K.C.C. Kharas, J.H. Lunsford, Catalytic partial oxidation of methane over $BaPbO_3$: possible involvement of peroxide ion, J. Am. Chem. Soc. 111 (1989) 2336–2337, https://doi.org/10.1021/ja00188a077.

[33] C.N.R. Rao, P. Ganguly, M.S. Hegde, D.D. Sarma, Holes in the Oxygen (2p) valence bands and the concomitant formation of peroxide-like species in metal oxides: their role in metallicity and superconductivity, J. Am. Chem. Soc. 109 (1987) 6893–6895, https://doi.org/10.1021/ja00256a076.

[34] C.S. Liang, L.J. Wu, J.M. Wu, Influence of forming Gas annealing on $BaPbO_3$/Pb(Zr,Ti)O_3/$BaPbO_3$ ferroelectric capacitors, Electrochem. Solid-State Lett. 8 (2005) 29–32, https://doi.org/10.1149/1.1979328.

[35] G. Suchaneck, A. Deyneka, L. Jastrabik, M. Savinov, G. Gerlach, Lead excess in Pb(Zr,Ti)O_3 thin films deposited by reactive sputtering at low temperatures, Ferroelectrics 318 (2005) 3–10, https://doi.org/10.1080/00150190590965901.

[36] M. Martos, J. Morales, L. Sánchez, Lead-based systems as suitable anode materials for Li-ion batteries, Electrochim. Acta. 48 (2003) 615–621, https://doi.org/10.1016/S0013-4686(02)00730-2.

[37] S.M. Wood, C.H. Pham, A. Heller, C.B. Mullins, Communication—stages in the dynamic electrochemical lithiation of lead, J. Electrochem. Soc. 163 (2016) A1027–A1029, https://doi.org/10.1149/2.1251606jes.

[38] P. Nithyadharseni, M.V. Reddy, K.I. Ozoemena, F.I. Ezema, R.G. Balakrishna, B.V.R. Chowdari, Electrochemical performance of $BaSnO_3$ anode material for lithium-ion battery prepared by molten salt method, J. Electrochem. Soc. 163 (2016) A540–A545, https://doi.org/10.1149/2.0961603jes.

[39] A. Débart, L. Dupont, P. Poizot, J.-B. Leriche, J.M. Tarascon, A transmission electron microscopy study of the reactivity mechanism of tailor-made CuO particles toward lithium, J. Electrochem. Soc. 148 (2001) A1266, https://doi.org/10.1149/1.1409971.

[40] X.Q. Zhang, X. Chen, X.B. Cheng, B.Q. Li, X. Shen, C. Yan, J.Q. Huang, Q. Zhang, Highly stable lithium metal batteries enabled by regulating the solvation of lithium ions in nonaqueous electrolytes, Angew. Chem. Int. Ed. 57 (2018) 5301–5305, https://doi.org/10.1002/anie.201801513.

[41] C. Barriga, S. Maffi, L.P. Bicceli, Electrochemical lithiation of Pb_3O_4, J. Power Sources. 34 (1991) 353–357, https://doi.org/10.1201/9781482293494-25.

[42] A. Zalkin, W.J. Ramsey, Intermetallic compounds between lithium and lead, J. Phys. Chem. 62 (1958) 689–693.

[43] M. Tathavadekar, S. Krishnamurthy, A. Banerjee, S. Nagane, Y. Gawli, A. Suryawanshi, S. Bhat, D. Puthusseri, A.D. Mohite, S. Ogale, Low-dimensional hybrid perovskites as high performance anodes for alkali-ion batteries, J. Mater. Chem. A. 5 (2017) 18634–18642, https://doi.org/10.1039/c7ta04529h.

[44] S.M. Wood, C.H. Pham, A. Heller, C.B. Mullins, Formation of an electroactive polymer gel film upon lithiation and delithiation of PbSe, J. Electrochem. Soc. 163 (2016) A1666–A1671, https://doi.org/10.1149/2.0961608jes.

[45] Q. Liu, S. Zhou, C. Tang, Q. Zhai, X. Zhang, R. Wang, Li-B alloy as an anode material for stable and long-life lithium metal batteries, Energies 11 (2018) 1–5, https://doi.org/10.3390/en11102512.